Article

A silver–copper oxide catalyst for acetate electrosynthesis from carbon monoxide

Roham Dorakhan [1,5], Ivan Grigioni [1,2,5], Byoung-Hoon Lee[1,5], Pengfei Ou [1], Jehad Abed [1], Colin O'Brien [3], Armin Sedighian Rasouli[1], Milivoj Plodinec [4], Rui Kai Miao [3], Erfan Shirzadi[1], Joshua Wicks [1], Sungjin Park[1], Geonhui Lee[1], Jinqiang Zhang [1], David Sinton[3] & Edward H. Sargent [1] ✉

Acetic acid is an important chemical feedstock. The electrocatalytic synthesis of acetic acid from CO_2 offers a low-carbon alternative to traditional synthetic routes, but the direct reduction from CO_2 comes with a CO_2 crossover energy penalty. CO electroreduction bypasses this, which motivates the interest in a cascade synthesis approach of CO_2 to CO followed by CO to acetic acid. Here we report a catalyst design strategy in which off-target intermediates (such as ethylene and ethanol) in the reduction of CO to acetate are destabilized. On the optimized Ag–CuO_2 catalyst, this destabilization of off-target intermediates leads to an acetate Faradaic efficiency of 70% at 200 mA cm^{-2}. We demonstrate 18 hours of stable operation in a membrane electrode assembly; the system produced 5 wt% acetate at 100 mA cm^{-2} and a full-cell energy efficiency of 25%, a twofold improvement on the highest energy-efficient electrosynthesis in prior reports.

The electrification of chemical and fuel production offers a way to reduce carbon emissions and contribute to a circular carbon economy[1–3]. The electrocatalytic CO_2 reduction reaction (CO_2RR) in electrolyser cells enables the production of valuable liquid hydrocarbons, such as ethanol, acetic acid and propanol. With a market size of US$13 billion and greenhouse gas emissions that average 1.8 kgCO_2e kg^{-1} acetic acid is a feedstock for the synthesis of polymers, textiles and solvents and is a precursor for food additives. Efficient electrochemical synthesis processes that rely on low-carbon (for example, wind generated) electricity have the potential to reduce this footprint by as much as one order of magnitude[4,5].

Generally, direct CO_2RR strategies suffer from CO_2 crossover to the anode, which leads to a large energy penalty from the associated CO_2 re-separation[6–8]. A cascade approach that started from a CO_2RR-to-CO process followed by a CO reduction reaction (CORR)-to-acetate one has seen encouraging progress and a reduced crossover penalty[9–14]. The realization of this technology for liquid hydrocarbon production hinges on improving the electrochemical CORR performance.

It is also imperative that liquid product mixtures—the combination of ethanol, acetate and propanol, for example—be delivered at high concentrations. This is due to the high separation costs associated with low-concentration electrolyte mixtures of liquid hydrocarbons (to illustrate, at concentrations below 1 wt%, >200 GJ ton$^{-1}_{acetate}$ of purification energy cost is estimated to be incurred (Supplementary Tables 1 and 2)). So far, the highest Faradaic efficiencies (FEs) to liquid products (C_{2+} liquid hydrocarbon reaching 55%) and the highest concentrations of liquid products (1 wt%) have yet to be united in a single high-FE, high-concentration system[15,16]. Here we aim to combine the catalyst and system design to both improve the reaction kinetics and minimize the liquid separation cost.

We posit a two-step acetic acid electrosynthesis approach and estimate that if a high energy efficiency (EE) is reached it will offer an about tenfold reduction of greenhouse gas emissions when powered by low-carbon (wind, 6 gCO_2e kWh^{-1}) electricity and using CO_2 (or CO derived therefrom) as feedstock (Fig. 1).

The CORR-to-acetate step needs improvement the most, and highlights the need for new catalyst designs. We began by synthesizing

[1]Department of Electrical and Computer Engineering, University of Toronto, Toronto, Ontario, Canada. [2]Dipartimento di Chimica, Università degli Studi di Milano, Milan, Italy. [3]Department of Mechanical and Industrial Engineering, University of Toronto, Toronto, Ontario, Canada. [4]ScopeM, ETH-Zürich, Zürich, Switzerland. [5]These authors contributed equally: Roham Dorakhan, Ivan Grigioni, Byoung-Hoon Lee. ✉e-mail: ted.sargent@utoronto.ca
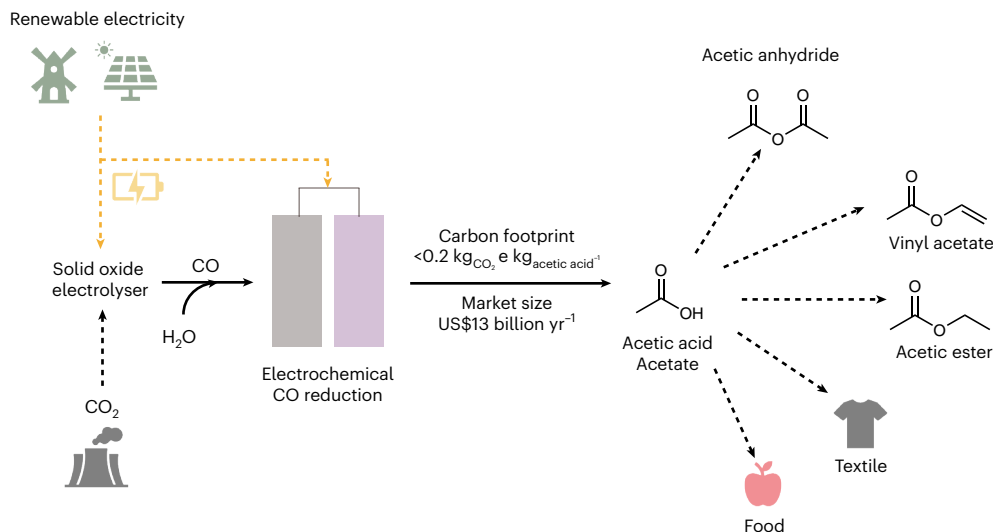
Fig. 1 | Acetic acid electrosynthesis. Chemical product chain of acetic acid electrosynthesis.

a series of Ag–Cu$_2$O catalysts using a kinetically restricted galvanic replacement strategy to vary the surface Ag content and produce different active-site landscapes. The Ag–Cu$_2$O catalysts reached an acetate FE of 70% at the optimal Ag:Cu loading, and a peak partial current density to acetate of 310 mA cm^{-2}. A combination of operando-Raman spectroscopy and density functional theory (DFT) calculations point to a destabilization mechanism that suppresses ethylene and ethanol formation, but leaves the acetate pathway accessible. By implementing the catalyst in a membrane electrode assembly (MEA), we achieved a full-cell EE (EE$_{FC}$) of 25.5%, accompanied by a sodium acetate concentration of 4.8 wt%. Energy analysis over the full acetic acid production pathway shows a cascade system that utilizes this CORR technology that has an overall energy intensity of 93 GJ ton$^{-1}_{acetate}$ (Supplementary Tables 1 and 2): this compares encouragingly with 560 GJ ton^{-1} (CO$_2$RR, bipolar) and 300 GJ ton^{-1} (CO$_2$RR, neutral) and is a major step towards replacing the current production methods.

Result and discussion

Synthesis and characterization of the Ag–Cu$_2$O

We initially posited that Ag is an ideal heteroatom dopant for Cu to enhance C$_{2+}$ selectivity in the CORR. This is due to: (1) the very low hydrogen evolution reaction (HER) activity of Ag and (2) Ag sits on the same side of the HER volcano plot as Cu, and so does not risk synergistic electronic interactions that would lead to an increase in HER[17,18]. Furthermore, we postulated that the population of surface CuAg sites and their Cu:Ag ratio to be a deciding factor in the catalyst performance. Hence, we started by developing a catalyst nanostructure in which we could tune the CuAg structure. Cu$_2$O nanoparticles (NPs) provided a platform for the control of the surface Ag concentration within the precatalyst via a galvanic replacement reaction. We synthesized porous Cu$_2$O NPs and employed a kinetically restricted galvanic replacement between Cu$_2$O and Ag$^+$ ions (Fig. 2a) to tune the distribution of Ag on the surface. In contrast to previous reports that show the formation of Ag NPs on the Cu surface during the galvanic replacement[19], when we restricted the replacement kinetics by controlling the Ag precursor concentration in the reaction mixture, we produced uniformly dispersed Ag on the Cu$_2$O surface. Scanning transmission electron microscopy (STEM) showed porous Cu$_2$O NPs ~100 nm in size that initially lacked Ag NPs up to an Ag concentration of 1% (Fig. 2b and Supplementary Figs. 1 and 2). When we introduced Ag beyond 1%, Ag NPs formed (namely, 2% Ag with an Ag NP diameter of 10–15 nm; Fig. 2c and Supplementary Figs. 3 and 4), and these were larger in the 5% Ag sample (50–60 nm; Supplementary Fig. 5). Energy dispersive X-ray spectroscopy (EDS) images of the 2 and

5% Ag samples showed that agglomerate particles on the Cu surface are Ag NPs. We then combined atomic resolution imaging high-angle annular dark-field (HAADF) STEM and EDS analysis using Cs-corrected STEM to visualize the Ag distribution on the Cu$_2$O surface (Fig. 2d and Supplementary Figs. 6–9). The presence of Ag NPs larger than 0.5 nm was absent up to Ag$_{1\%}$–Cu$_2$O, with the Ag NP formation being observed above this Ag loading. HAADF STEM and EDS analysis on the Ag-NP-free surface of Ag$_{2\%}$–Cu$_2$O confirmed that Ag exists as uniformly distributed Ag, even when Ag NPs are formed. In X-ray diffraction, Ag metal peaks, such as (111), (200) and (220), emerge above a 2% Ag concentration (Fig. 2e). Ag K-edge X-ray absorption near-edge structure (XANES) fluorescence spectroscopy showed a characteristic metallic Ag absorption edge of 25,520 eV, which indicates that Ag is in a metallic state for all the Ag concentrations (Fig. 2f)[19].

High-resolution X-ray photoelectron spectroscopy (XPS) indicated metallic Ag (Supplementary Fig. 10). Cu K-edge XANES and EXAFS (extended X-ray absorption fine structure) fluorescence spectra of the Ag-containing catalysts revealed that the surface Cu in the unreacted electrodes was in the +1 oxidation state (Supplementary Figs. 11 and 12).

CO electroreduction performance of Ag–Cu$_2$O

We used a flow cell with a gas diffusion layer (GDL) to study the electrocatalytic performance operating at >100 mA cm^{-2} current density (Supplementary Fig. 13)[20]. The Ag–Cu$_2$O precatalysts reduced to metal Ag–Cu alloys under CORR conditions (Supplementary Figs. 35 and 36)[21]. We measured the electrochemical surface area of pure Cu$_2$O and Ag$_{1\%}$–Cu$_2$O following chronopotentiometry at 100, 200, 300 and 400 mA cm^{-2} (Supplementary Figs. 14–17). The electrochemical surface area reaches its maximum at higher potentials and remains high even when brought to a lower potential afterward (Supplementary Fig. 18 and Supplementary Note 3). All the CORR performance measurements were hence taken after the catalysts reached their highest electrochemical surface area.

Figure 3a shows the FEs of the CORRs for various Ag–Cu$_2$O samples at 100 mA cm^{-2} and 1 M KOH. The pure Cu$_2$O-derived catalyst (referred to as Cu$_2$O from now on) shows the lowest acetate FE of 10% and achieves a high C$_{2+}$ FE of 85%. Oxide-derived Cu enables C–C coupling from the abundance of grain boundaries formed during the in situ reduction[22–24]. As the Ag concentration increased in the Ag–Cu$_2$O samples, the acetate productivity increased at the expense of hydrogen, ethylene and ethanol. The decrease in ethylene and hydrogen FE from 40 to 35% and 15 to 13%, respectively, was accompanied by an increase in acetate from 10
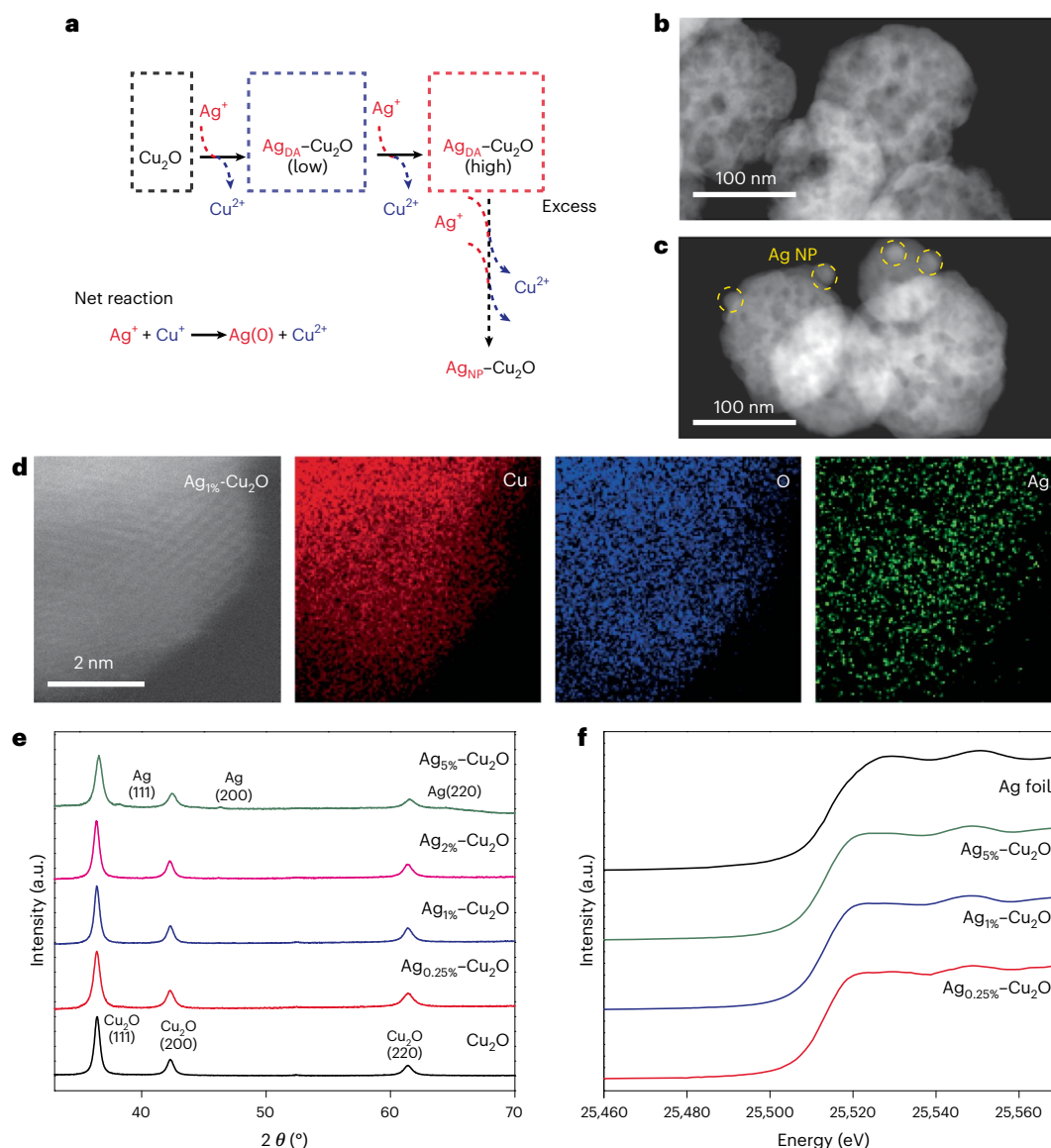
Fig. 2 | Synthesis and characterization of Ag–Cu$_2$O catalysts. a, Synthetic scheme for the AgCu dilute alloy (DA) bimetallic catalyst materials through a galvanic replacement reaction. **b,c**, STEM image of Ag$_{1\%}$–Cu$_2$O (**b**) and Ag$_{2\%}$–Cu$_2$O (**c**). **d**, High-resolution Cs-corrected HAADF STEM–EDS image of the Ag$_{1\%}$–Cu$_2$O catalyst showing a uniform Ag distribution. **e,f**, X-ray diffraction patterns (**e**) and Ag K-edge XANES spectra (**f**) of AgCu bimetallic catalysts with different Ag concentrations. a.u., arbitrary units.

to 15%. This change in C$_2$ selectivity with increased Ag loading points to CuAg active sites with a different selectivity towards C$_2$ products than towards Cu. This was further reflected in the 1% Ag loading sample, in which there was a dramatic change in FE distribution. The ethylene was reduced to ~22% with a sharp increase in acetate to 55%. The types of CuAg sites at this Ag loading and their relative population suppressed the formation of ethanol and ethylene, and promoted the formation of acetate. With an increased Ag loading to 2%, agglomerated Ag NPs were observed (Fig. 2c and Supplementary Figs. 8 and 9) on the Cu$_2$O, as reflected in the FE distribution in which ethylene and ethanol FE start to increase and acetate begins to be suppressed. Supplementary Fig. 19 shows the FE distribution of all the Ag–Cu$_2$O samples at 100, 200, 300 and 400 mA cm^{-2}, whereas the performance of a commercial CuAg alloy catalyst produced a >50% FE towards H$_2$ (Supplementary Fig. 20). This shows that the CuAg sites formed prior to the Ag NP formation produce acetate and suppress other C$_2$ formations. Furthermore, to probe the Ag loading at which the population of these sites is maximized, we performed CORRs on samples with 0.75 and

1.25% Ag loading (Supplementary Fig. 21), which showed 1% Ag with the highest FE towards acetate and, hence, the highest population of acetate-producing CuAg sites.

The potential dependence of the Ag$_{1\%}$–Cu$_2$O sample FE is shown in Fig. 3b. Increasing the current density from 100 to 200 mA cm^{-2} caused the FE to C$_{2+}$ products to increase. This was accompanied by a drop in the HER FE, with no increase in CH$_4$ FE. At this current density, the C$_2$ product distribution shifted towards a higher acetate, and peaked at an FE of 70%. Further increases of the current density resulted in the increase of ethanol. It was also at this potential that CH$_4$ formation reached detectable limits, an indication of the depletion of the surface CO. This was confirmed by the increase in CH$_4$ and HER at 400 mA cm^{-2} and a decrease in C$_{2+}$. The FE to acetate remained high at a large current density with a peak $J_{acetate}$ of 310 mA cm^{-2} (Supplementary Fig. 22).

Figure 3c–e shows the partial current densities of the C$_2$ products versus half-cell potentials (iR corrected). The ethylene and ethanol partial current densities of the 0.25 and 0.5% Ag samples are below that of Cu$_2$O, which shows that at low surface coverages, Ag acted as
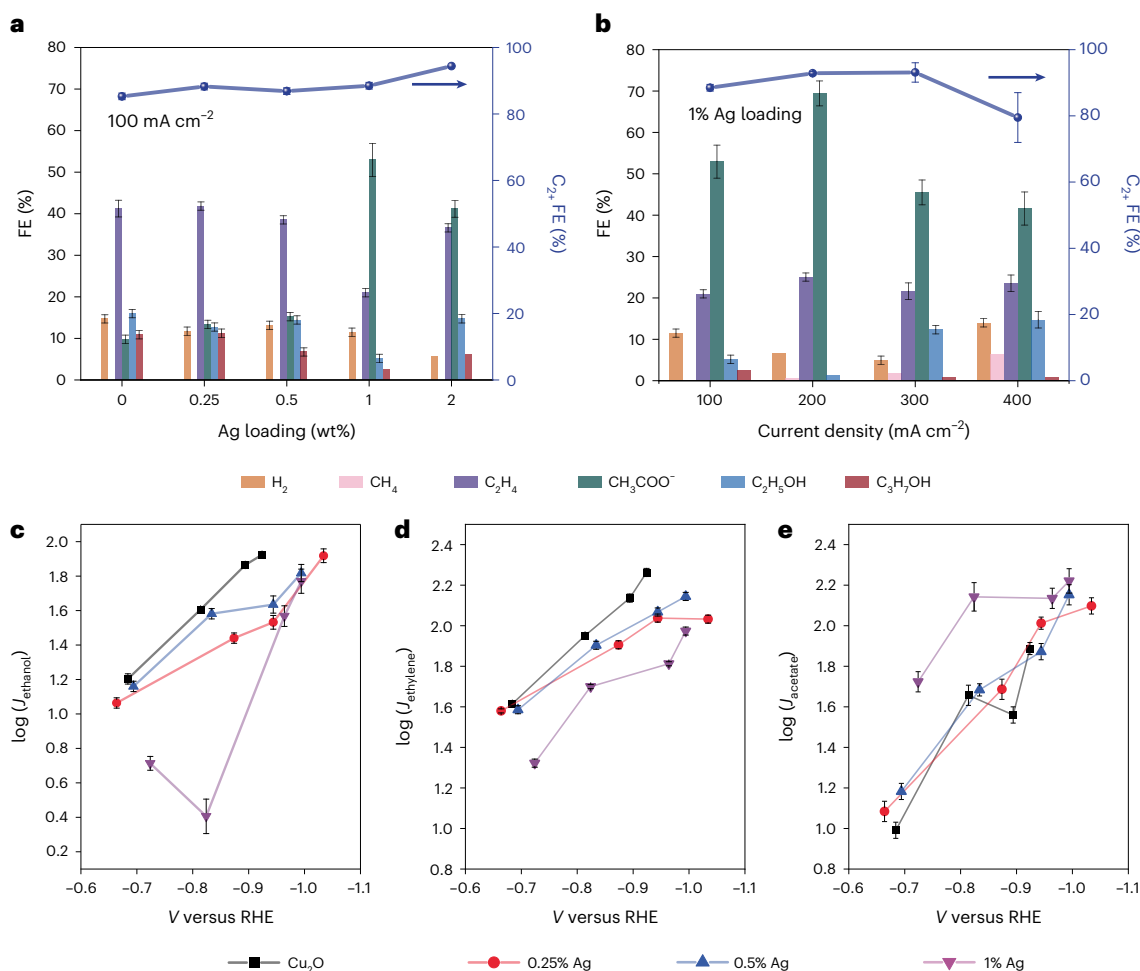
Fig. 3 | Electrochemical performance measurement of Ag–Cu₂O series. a, FEs of hydrogen, methane, ethylene, acetate, ethanol and propanol during CO electroreduction at 100 mA cm⁻² in a three-electrode flow cell. **b**, FE distribution of the CORR products for the Ag₁%–Cu₂O catalyst at different current densities. **c–e** Ethanol (**c**), ethylene (**d**) and acetate (**e**) partial current densities of C₂ products for the Cu₂O and 0.25, 0.5 and 1% Ag–Cu₂O catalysts. All the error bars correspond to n = 3 measurements. Data are presented as the mean value (n = 3) and the error bars correspond to the range of the dataset.

an inhibitor to these product pathways. In the 1% Ag sample, the same inhibitory trend of $J_{ethylene}$ continued and reached its lowest value. In the case of ethanol, this inhibition was exaggerated at lower potentials (Fig. 3c). The abundance of CuAg sites at this Ag loading dictated the FE distribution, and the ethanol pathway was destabilized to a point at which larger reductive potentials are needed to enable access to this product.

The partial current density of acetate remained relatively unchanged across all Ag loadings. This shows that the new CuAg site did not enhance the production rate of acetate, but rather inhibited the competing product pathways, which enhanced the reaction selectivity towards acetate. In the 1% Ag sample, there was a slight increase in $J_{acetate}$ at lower potentials (Fig. 3e). This is attributed to a decrease in the HER at those potential ranges, which resulted in more J_{C_2} and, by extension, a higher $J_{acetate}$. At higher potentials (<−0.9 versus the reversible hydrogen electrode (RHE)), the $J_{acetate}$ of the 1% Ag became equal to those of its lower Ag loading counterparts.

DFT calculations

To investigate the nature of this destabilization mechanism, we employed DFT models of pure Cu and surface alloy CuAg systems. We first investigated the difference in the energetics of the ethylene and ethanol pathways versus the acetate pathway on the C–C coupling active slab of Cu(100) (Fig. 4). We found that the most favourable pathway towards C–C coupling went through OCCOH*

(Fig. 4a, intermediate I.1), in which the subsequent proton-coupled electron transfer dictated the pathway towards either ethylene or ethanol via HOCCOH*, or acetate via CCO* (intermediates I.2 and A.1, respectively; Fig. 4a)[25–28]. This points to HOCCOH* as the intermediate that diverged the ethanol–ethylene pathway from the acetate pathway. Controlled destabilization can thus produce conditions wherein the HOCCOH* evolution is endergonic, whereas the CCO* remains exergonic.

Substitution of the surface atoms with heteroatoms in bimetallic alloys modulates the electronic configuration of the surrounding atoms. Ag has a lower CO* binding energy than Cu, and hence has the potential to destabilize all intermediates along the OCCOH* pathway. We simulated a series of AgCu surfaces with different Ag:Cu ratios (Fig. 4b and Supplementary Figs. 23–31) and recalculated the energy along both pathways on these slabs (Fig. 4c,d and Supplementary Tables 3–10), along with the CO* adsorption energy (Supplementary Fig. 32). We found that the addition of Ag, even at a Ag₁Cu₈ surface coverage, destabilized the HOCCOH* and CCO* pathways; however, both pathways remained exergonic and accessible. In the cases of Ag₂Cu₇ and Ag₃Cu₆, with a higher Ag content, the HOCCOH* pathway became endergonic, whereas the CCO* pathways remained exergonic. It is in this regime of the Ag:Cu ratio that one may suppress the formation of ethylene and ethanol while keeping the acetate pathway energetically accessible, which suggests a route to enhanced acetate FE.
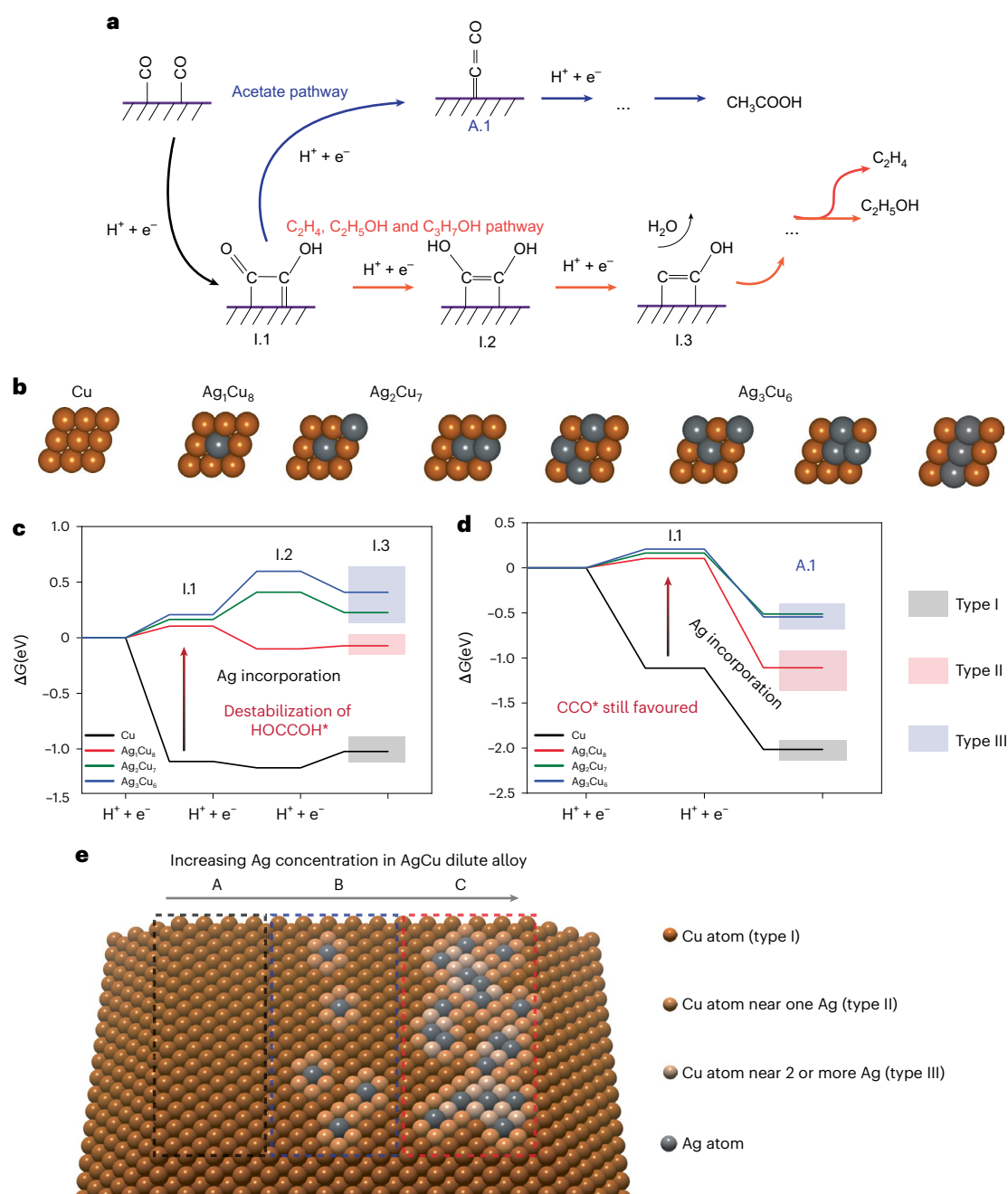
Fig. 4 | Computational studies of C_2 pathways on AgCu slabs. a, Reaction pathways for ethylene, ethanol and acetate production in the CORR, where I.1 is OCCOH*, I.2 is HOCCOH*, I.3 is CCOH* and A.1 is CCO*. **b**, Different AgCu slabs used to simulate the reaction pathway of the C_2 product in the CORR. **c,d** Gibbs free energy change of the reaction pathway towards ethylene and ethanol through HOCCOH* (**c**), and towards acetate through CCO* (**d**) for different AgCu slabs. **e**, The Ag content in AgCu surface alloys gives rise to different active sites and their distribution.

We identified distinct reaction regimes as a function of Ag content, and refer to their active sites as type I (pure Cu), type II (one Ag neighbour, Ag_1Cu_8) and type III (more than one Ag neighbour, for example, Ag_2Cu_7 and Ag_3Cu_6). Figure 3e shows the evolution of new active sites moving from I through II to III and the increase in their relative populations with increased surface Ag content. Two factors controlled the intensity of the change in product distribution: (1) the electronic difference of the new active sites from the pure Cu sites and (2) the relative distribution of these active sites versus that of the pure Cu sites.

Through control over the surface distribution of the Ag atoms in the Ag–Cu_2O catalysts, we were able to change the relative distribution of type I and type II and/or III sites. Lower Ag loading samples were

populated with type I sites, whereas an increased Ag loading gave rise to type II and/or III sites and eventually made these sites the predominant active sites for the CORR. Experimentally, this confirms the high FE of acetate shown for the 1% Ag loading sample, in which the Ag distribution is very high, and the Ag atoms are atomically dispersed. This sample has an abundance of type II and/or III sites, which destabilizes all the non-acetate C_2 pathways.

Operando and post-catalysis characterizations

We used operando Raman spectroscopy to interrogate the surface species during CORRs under different potentials and identified the bound intermediates that led to C_{2+} products at a molecular level[29].
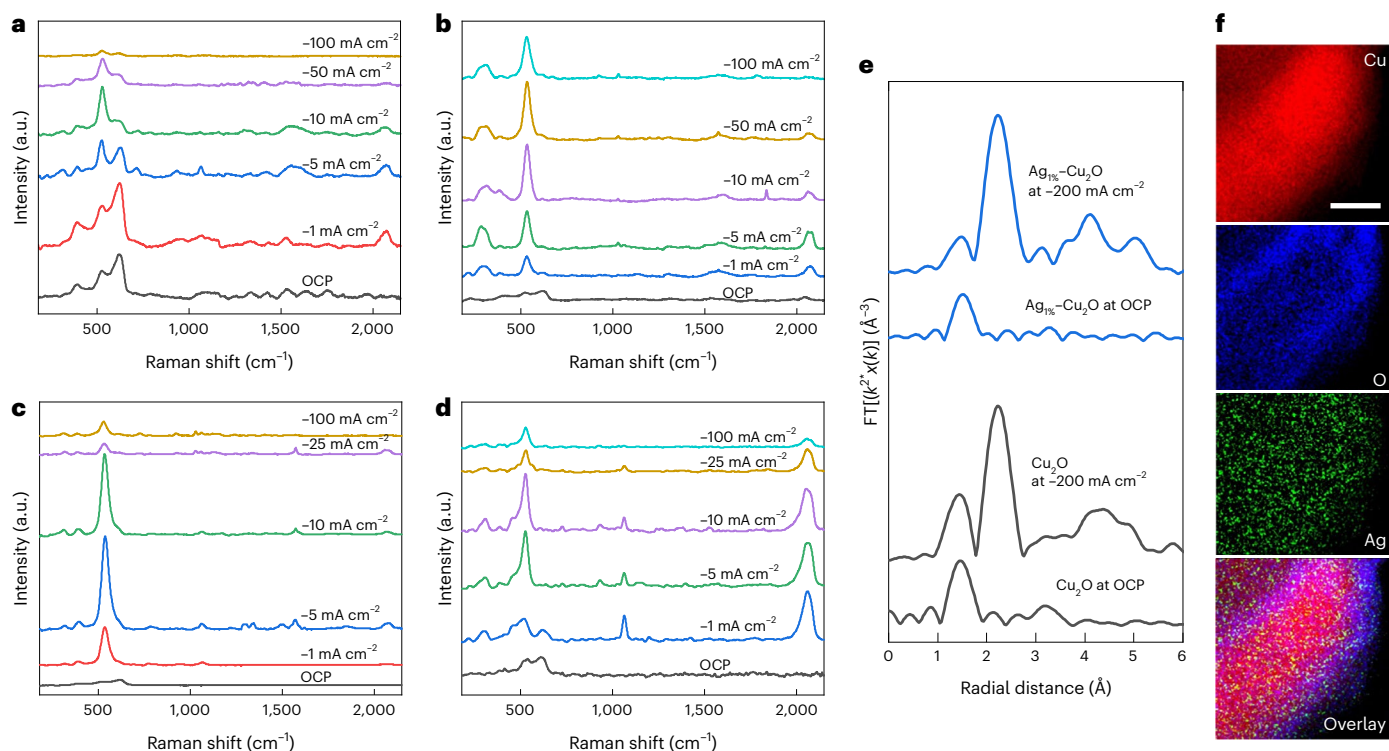
Fig. 5 | a–d, Operando Raman spectroscopy studies of Cu_2O (a), $Ag_{0.5\%}$–Cu_2O (b), $Ag_{1\%}$–Cu_2O (c) and $Ag_{2\%}$–Cu_2O (d) in a flow cell with the electrodes in contact with 1 M KOH. The spectra were collected in the chronopotentiometry mode. **e**, Operando Cu K-edge EXAFS of Cu_2O and $Ag_{1\%}$–Cu_2O spectra collected before starting the CORR and under a CORR at −200 mA cm⁻². **f**, High-resolution transmission electron microscopy with EDS mapping at an atomic resolution of $Ag_{1\%}$–Cu_2O after a CORR. Scale bar, 10 nm. OCP, open circuit potential.

As we stepped the current below −1 mA cm⁻² (Fig. 5a–d), the Cu oxide peaks disappeared (Fig. 5a–d and Supplementary Fig. 33), and a broad feature of atop-bound CO* appears, with a peak of 2,065 cm⁻¹. The signal intensity under low current densities (−5 mA cm⁻²) is representative of the CO* saturation coverage[30]. At this current density, the presence of type II and/or III active sites with few Ag atoms on the surface in $Ag_{0.5\%}$–Cu_2O increased the *CO coverage, and two new adsorption modes appeared: a Cu–CO frustrated rotation (the broad feature peaking at 290 cm⁻¹) and a new peak of atop Ag–CO (the sharp peak at 535 cm⁻¹) (refs. [19,31–34]). With more type II and/or III sites in $Ag_{1\%}$–Cu_2O, the Cu–CO frustrated rotation feature was more defined and associated with the Cu–CO stretching signal at 380 cm⁻¹. In the Raman spectra, the bands of Cu–CO frustrated rotation and stretching shifted to higher frequencies compared with the literature values. This shift indicates a stronger Cu–CO bond which may favour C–C coupling[35,36]. Larger Ag amounts (for example, 2%) increased atop-bound CO*, which peaked at 2,065 cm⁻¹ and the sharp Ag–CO peak at 535 cm⁻¹ (Fig. 5) shows a shoulder at 480 cm⁻¹ associated with adsorbed CO on the bulk Ag of AgNPs[32].

We observed additional sharp bands in the 700–1,600 cm⁻¹ region when type II and/or III active sites were available at an Ag content above 1%. Control experiments with argon showed that these peaks arise during the CORR (Supplementary Fig. 34). These Raman modes are associated with acetate-specific intermediates, such as the vibration modes of carboxylate (COO–) and other C_2 intermediates (Supplementary Fig. 35)[29,37–39]. Their intensification indicated a larger abundance of stabilized acetate intermediates on $Ag_{1\%}$–Cu_2O and $Ag_{2\%}$–Cu_2O as the number of type II and/or III sites increased. Atop CO* is a key species towards C_{2+}, and the additional coverage of Ag–CO favours a high selectivity towards C_{2+} (ref. [40]). As we stepped to more negative current densities, the intensity of the adsorbed intermediates decreased due to their progressive consumption and the formation of bubbles.

We performed operando X-ray absorption experiments to investigate the local electronic nature of the catalysts during the CORR. Operando-XANES on the Cu K edge in the Cu_2O and Ag1%–Cu_2O samples indicated that the Cu is in the metallic state during the CORR (Supplementary Fig. 36). Operando EXAFS showed that the local structure of Cu is unaltered by the presence of surface Ag, which we attribute to the large Cu to Ag ratio in the catalysts. We examined the spent $Ag_{1\%}$–Cu_2O catalyst with HAADF-STEM with EDS mapping after the CORR (Fig. 5f and Supplementary Figs. 37 and 38). After the CORR, the Ag was still uniformly distributed on the Cu_2O surface without signs of agglomeration. Moreover, oxygen was then distributed at the surface, as seen by the blue right edge of the NP (Fig. 5f), which confirmed that during the CORR, Cu_2O undergoes reduction followed by surface oxidation in the air after we turned off the reaction.

These spectroscopic observations revealed that the presence of surface Ag atoms on Cu_2O allows modulation of the adsorption of the CORR intermediates by regulating the Ag loading. The presence of new active sites promoted the surface CO dimerization by suppressing the competing HER reaction, and the preferential destabilization of intermediates along the ethylene and ethanol pathway promoted acetate selectivity through the *CCO intermediate, as supported by the DFT study. Operando XAS and EDS mapping on spent samples showed that the catalyst retained its atomic-scale architecture during the catalysis.

MEA systems

We further demonstrate the applicability of the catalyst in a zero-gap MEA similar to that used by Ripatti et al.[16]. Recent studies by Zhu and Wang highlighted the importance of product concentration in the CO_2RR and the CORR[41]. However, minimization of the electrical energy input in a CORR system is needed due to the preceding CO_2-to-CO
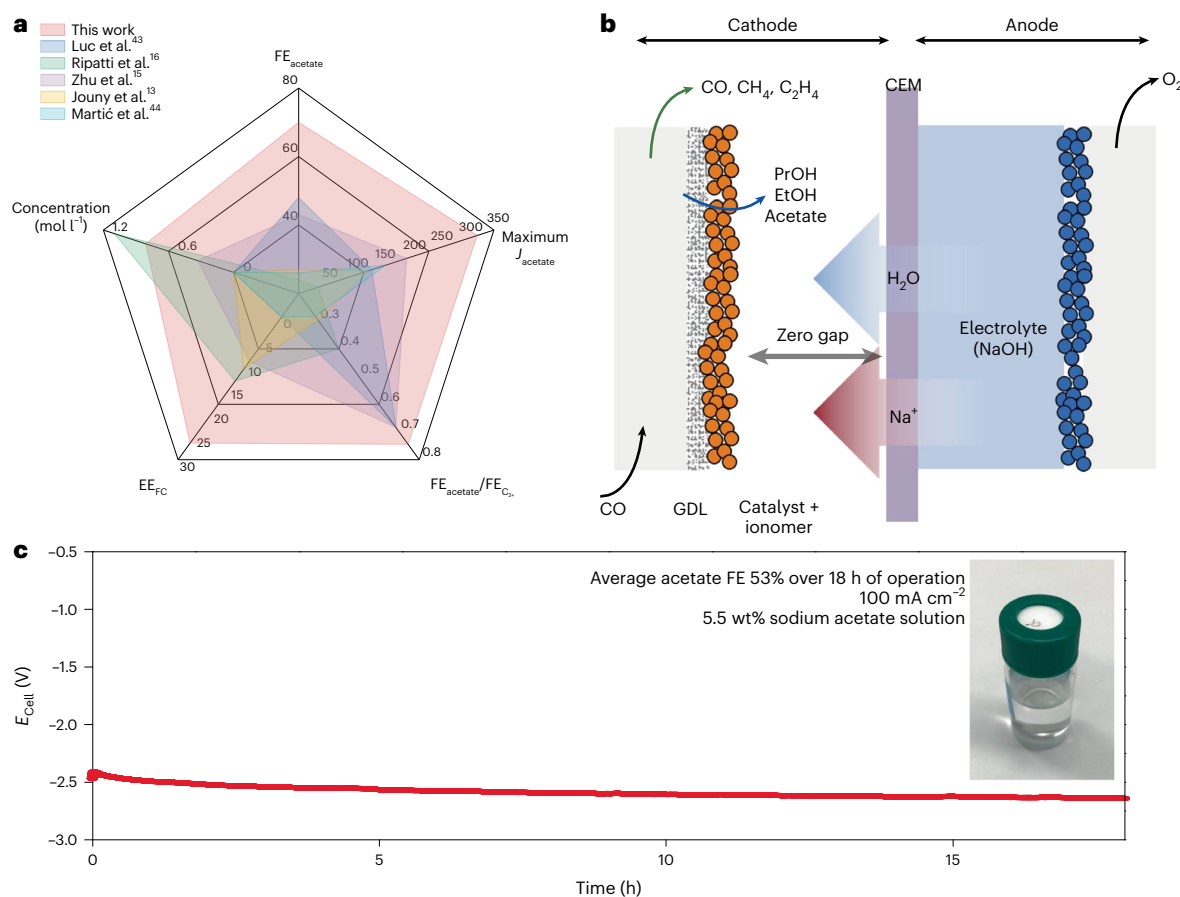
Fig. 6 | Acetate production activity of an Ag–Cu$_2$O catalyst and concentrated acetate production in MEA applications. a, Comparison of the performance metrics of this work and other relevant references. **b**, Schematic image of a MEA application. **c**, Chronopotentiometry stability test of Ag$_{1\%}$–Cu$_2$O at 100 mA cm^{-2} in MEA with a product concentration of 5.5 wt% (0.9 M). CEM, cation-exchange membrane.

endothermic step when compared with that of a direct CO$_2$RR. Therefore, the targets of liquid concentration and low full-cell voltage (V_{FC}) at industrially relevant current densities need to be met within the same system. Figure 6a compares the performances here (both flow cell and MEA) with those of prior work. The Ag–Cu$_2$O catalyst exhibits the highest acetate FE reported, and it shifts the C$_2$ product pathway to acetate (FE$_{acetate}$/FE$_{C_2}$) (Supplementary Table 10). Using the zero-gap system of Fig. 6b and a circulating 1 M NaOH solution as the anolyte enabled a ~4.8 wt% sodium acetate solution with a stable operation over 18 hours at a 2.5 V full-cell potential and 100 mA cm^{-2} (Fig. 6c). This corresponds to an EE$_{FC}$ of 25.5% (refs. [15,41]).

Conclusion

In this work, we demonstrated a two-step electrosynthesis approach for the production of acetic acid with a tenfold lower carbon footprint. The family of Ag–Cu$_2$O alloy NP precatalysts with different Ag loadings enabled inhibition, operando, of the formation of ethylene and ethanol, which resulted in an acetate FE of 70% at 200 mA cm^{-2}. Computational studies, electrochemical measurements and operando Raman spectroscopy elucidated the role of Ag incorporation onto Cu in selective acetate production. We provide evidence that the presence of Ag and the active sites that surround Ag atoms destabilizes the ethanol and ethylene pathway in the CORR while maintaining the exergonicity of the acetate pathway. The catalyst in a zero-gap MEA system enabled a ~5 wt% sodium acetate solution over 18 hours of stable operation with an EE$_{FC}$ of 25.5% at 100 mA cm^{-2}.

Methods

Preparation of catalyst and gas diffusion electrode

Materials. Cu(CH$_3$COO$^-$)$_2$, aqueous N$_2$H$_4$ solution (35 wt%), AgNO$_3$, ethanol, HCl (37 wt%), KOH, dimethyl sulfoxide, deuterated water, polytetrafluoroethylene (PTFE) NPs (Nanoshel, 350–400 nm) and methanol were used as purchased from Sigma Aldrich. CO (grade 4) was purchased from Praxair and Ar (grade 5) was purchased from Messer. Nickel foam was purchased from MTI Corporation. The carbon-based gas diffusion electrode (GDE; Freudenberg H23C9), anion exchange membrane (Fumasep FAA-PK-130), Nafion 212 and 5% Nafion perfluorinated resin solution 5 wt% (D520, EW = 1,000) were purchased from the Fuel Cell Store. Deionized water (18.2 MΩ) was used in all the experiments.

Synthesis of electrocatalysts

The synthesis of Ag–Cu$_2$O catalysts with various concentrations followed a two-step procedure[42]. The first step is the synthesis of porous Cu$_2$O NPs, modified from the previously reported method. Cu(CH$_3$COO$^-$)$_2$ (200 mg) was dissolved in 80 ml of H$_2$O. N$_2$H$_4$ solution (of 35 wt%, 300 µl) was added dropwise to the aqueous Cu acetate solution. Note that the N$_2$H$_4$ solution is a strong reductant and should be added very slowly, and the Cu acetate solution should be vigorously stirred to prevent agglomerated Cu NP formation. HCl solution (2 M, 1 ml) was added dropwise to the reaction mixture and magnetically stirred for 30 min. The reaction mixture was centrifuged and washed with water and ethanol twice to obtain porous Cu$_2$O NPs. The second step was a kinetically controlled galvanic replacement reaction between Cu$_2$O and Ag$^+$ cations.

Porous Cu_2O NPs were dispersed in 30 ml of H_2O. An aqueous $AgNO_3$ solution of 1 mg ml^{-1} concentration was prepared. The calculated amount of $AgNO_3$ solution (for example, 0.98 ml for 1%) was added slowly, dropwise, for 2 h into a vigorously stirred aqueous Cu_2O solution. The reaction mixture was vigorously stirred for an additional 30 min, then washed in water and lyophilized to obtain the final Ag–Cu_2O catalysts.

Preparation of gas-diffusion electrode

The catalyst was deposited on a Freudenberg H23C9 GDE using an air-brush technique, with GDE dimensions of (3×3 cm^2) or (2×2 cm^{-2}). The ink was composed of the catalyst NPs (Cu_2O and Ag–Cu_2O), 5% Nafion solution, PTFE NPs and 5 ml of methanol. The ink composition was chosen to obtain a 0.8 mg cm^{-2} catalyst loading with a Nafion content of 40 μl$_{Nafion}$:1 mg$_{catalyst}$ and a PTFE NP content of 1 mg$_{PTFE\_NP}$:1 mg$_{catalyst}$. The ink was vortexed for 5 min and sonicated for more than 1 h before being deposited on the GDE. For the electrode samples used in the MEA set-up, the PTFE NPs were omitted from the ink composition. The electrode was left under room conditions overnight before the electrochemical measurements were conducted.

Structural characterization

TEM imaging was conducted on a JEOL EM-2010 microscope operated at 200 kV. STEM imaging and EDS measurements were performed in the STEM mode equipped with a single drift detector (X-MAX^N, Oxford Instruments). SEM imaging was conducted on a Hitachi FE-SEM SU5000 microscope operated at 30 kV. The powder samples were deposited on a carbon tape before SEM imaging. XRD analysis was performed on a MiniFlex600 system that employed Cu Kα radiation. XPS measurements were conducted using the PerkinElmer model 5600, equipped with a 1,486.6 eV monochromated Al Kα X-ray source. The samples were prepared on conductive glass substrates by drop casting a few droplets of ink solution.

High-resolution transmission electron microscopy measures at the atomic scale were carried out at the ScopeM facility ETH-Zurich by employing a JEOL JEM-ARM300F Grand ARM 'Vortex' operated at 200 kV in the STEM mode. EDS mapping was performed on dual large-area SDD EDX detectors with 100 mm^2 of active area, a total solid angle of 1.6 sr and an energy resolution of $\leq$133 eV for Mn Kα. The annular bright field inner and outer semi-angles were set to 12 and 24 mrad, respectively. The HAADF inner and outer semi-angles were set to 64 and 180 mrad, respectively.

Electrochemical CO reduction measurements

Electrochemical rate measurements were performed in both a flow cell and the MEA configuration. For the flow-cell set-up, the catalyst-deposited GDE was used as the working electrode (cathode) and nickel foam as the counter electrode (anode). An anion exchange membrane (Fumasep FAA-PK-130) was used to separate the anodic and cathodic compartments. The flow cell assembly constituted the GDE, anion exchange membrane and nickel anode, and the liquid electrolyte (1 M KOH) was circulated in both anodic and cathodic compartments using a peristaltic pump (McMaster-Carr). Carbon monoxide was passed behind the GDE using a mass flow controller (Sierra Smart-Track 100), with an Ag/AgCl reference electrode inserted inside the cathodic compartment for the half-cell potential measurement. For the MEA set-up, the catalyst-deposited GDE was used as the working electrode (cathode) and an IrO$_2$–Ti felt (Sigma Aldrich) as the anode. A Nafion 212 cation-exchange membrane was used to keep a separation between the anolyte and the cathodic liquid products. The MEA was assembled by layering the GDE, Nafion and IrO$_2$–Ti felt and pressing them between the cathode plate (1 cm^2 flow field, stainless steel) and the anode plate (5 cm^2 titanium, flow field). A 1 M NaOH solution was circulated through the anodic flow field using a peristaltic pump, and CO was flown into the cathodic flow field using a mass flow controller. The liquid products were collected inside a cooled container (2–6 °C)

from the outlet of the cathode plate. For both configurations, the CO flowrate was 25–40 sccm and the electrolyte flow was 10–15 ml min^{-1}. Electrochemical reactions were performed using an electrochemical workstation (Autolab PGSTAT302N) connected to a current booster (Metrohm Autolab, 10A). Electrode potentials were rescaled to the RHE reference by:

$$E_{\text{versus RHE}} = E_{\text{versus Ag/AgCl}} + 0.235 V + 0.059 \times \text{pH}$$

An electrochemical impedance spectroscopy measurement using an Autolab PGSTAT302N electrochemical workstation was performed to obtain a cell resistance of 3.51 Ω. iR corrections to the potential were then performed using the equation:

$$E_{iR \text{ free}} = E_{\text{versus Ag/AgCl}} - 0.85 R_{\text{cell}} i_{\text{cell}}$$

where $E_{iR \text{ free}}$ is the corrected potential at the cathode, $E_{\text{versus Ag/AgCl}}$ is the applied potential and i_{cell} is the total current (a negative value at the cathode). A correction factor of 0.85 was used due to the 1 M KOH electrolyte's high conductance and low voltage drop across the electrolyte.

The EE$_{FC}$ of the MEA system was obtained from the equation:

$$\text{EE}_{\text{FC}} = \text{FE}_{\text{acetate}} \times \frac{E^{\circ}_{\text{cell}}}{V_{\text{FC}}}$$

where FE$_{\text{acetate}}$ is the system's FE towards acetate, and V_{FC} is the average full-cell voltage over the length of the stability experiment. The standard reduction potential of the cell was obtained from the standard Gibbs free energy of the reaction $2CO + 2H_2O \rightarrow CH_3COOH + 2O_2$:

$$E^{\circ}_{\text{cell}} = \frac{-\Delta G^{\circ}_{2CO+2H_2O \rightarrow \text{acetate}+2O_2}}{zF}$$

where z is equal to 4 and F is the faraday constant, 96,485 C mol^{-1}.

Product analysis

The gas products from the CORR were analysed by sampling 1 ml of the electrolyser outlet gas with an air-tight syringe (Hamilton, 5 ml). The gas sample was injected into a gas chromatograph (Shimadzu GC-2014) equipped with a thermal conductivity detector and a flame ionization detector. A Molecular Sieve 5A and Carboxen-1000 column were installed upstream from the thermal conductivity and flame ionization detectors, respectively, to separate the H_2, CO and gaseous hydrocarbons. The liquid products were quantified using NMR spectroscopy and HPLC. A 1 ml sample of the electrolyte was taken at various times during the reaction. ^{1}H NMR spectra of the analyte samples were taken using an Agilent DD2 600 spectrometer with dimethyl sulfoxide as an internal standard. For accurate measurements of the acetate concentration, an HPLC equipped with a HPX87H Aminex column (Bio-Rad) was calibrated for acetate. The results from both the HPLC and NMR were within a 5% error. The FE of the CORR gas product was calculated by the equation:

$$\text{FE}_{i,\text{gas}} = y_{i,\text{gas}} \dot{V} z_i F \frac{P_0}{RT} j_{\text{total}}$$

where y_i is the volume fraction of gas product i, $\dot{V}$ the outlet gas flow rate in sccm, z_i the number of electrons associated with producing one molecule of i, F the Faraday constant, P_0 the atmospheric pressure, R the ideal gas constant, T the temperature and j_{total} the total current density. The FE of the liquid product was calculated using the equation:

$$\text{FE}_{i,\text{liquid}} = n_{i,\text{liquid}} z_i F \frac{1}{Q_{\text{total}}}$$

where n_i is the number of moles of liquid product i, and Q is the total charge passed prior to the liquid sample being taken.

Electrochemical characterization

Cyclic voltammetry characterization with electrodes assembled in a flow cell was performed with the same equipment used for the CORR experiments. *iR* correction of the applied potential was not performed.

Operando and ex situ spectroscopic analysis

Operando and ex situ XAS Cu K-edge measurements were carried out at the European Synchrotron Radiation Facility at beamline ID26, which is equipped with high-energy-resolution fluorescence detectors. We used a flow-cell electrolyser modified to host an X-ray transparent window that faced the cathode backside. Ag K-edge and Cu K-edge experiments were conducted at beamline 9MB of the Advanced Photon Source at the Argonne National Laboratory and the Canadian Light Source.

Operando Raman spectroscopy was operated with a water immersion objective using a Renishaw inVia Raman microscope. The spectra were collected using a 785 nm laser. To avoid damaging the samples, the full spectrum was collected in two ranges (centred at 700 and 1,700 cm^{-1}) using a 0.05% full laser intensity, 0.1 s integration time and 200 repetitions. The raw data were base corrected manually by using Origin 2019 software. An open-structured flow cell was utilized for the measurements. An Ag/AgCl electrode (filled with saturated aqueous KCl solution) and a platinum wire were used as the reference and counter electrode, respectively. We collected the spectra at different current densities for each catalyst to allow a comparison between the different Ag percentages that was free of differences due to the mass transport phenomena of surface species.

Computational methods

All DFT calculations in this work were carried out using a periodic slab model with the Vienna ab-initio simulation program (https://www.vasp.at/). The Supplementary Information provides detailed information on the calculations and the derivation of the Gibbs free energy for elementary steps.

Data availability

Source data are provided with this paper. All the other relevant data supporting the findings of this study, which include techno-economic assessment methodologies, computational details and other experimental, microscopic and spectroscopic analyses, are available within the article and its Supplementary Information.

References

1. Schiffer, Z. J. & Manthiram, K. Electrification and decarbonization of the chemical industry. *Joule* **1**, 10–14 (2017).
2. Luderer, G. et al. Impact of declining renewable energy costs on electrification in low-emission scenarios. *Nat. Energy* **7**, 32–42 (2022).
3. Tackett, B. M., Gomez, E. & Chen, J. G. Net reduction of CO₂ via its thermocatalytic and electrocatalytic transformation reactions in standard and hybrid processes. *Nat. Catal.* **2**, 381–386 (2019).
4. Le Berre, C., Serp, P., Kalck, P. & Torrence, G. P. in *Ullmann's Encyclopedia of Industrial Chemistry* (2014); https://doi.org/10.1002/14356007.A01_045.PUB3
5. Medrano-García, J. D., Ruiz-Femenia, R. & Caballero, J. A. Revisiting classic acetic acid synthesis: optimal hydrogen consumption and carbon dioxide utilization. *Comput. Aided Chem. Eng.* **46**, 145–150 (2019).
6. Alerte, T. et al. Downstream of the CO₂ electrolyzer: assessing the energy intensity of product separation. *ACS Energy Lett.* **6**, 4405–4412 (2021).
7. Mardle, P., Cassegrain, S., Habibzadeh, F., Shi, Z. & Holdcroft, S. Carbonate ion crossover in zero-gap, KOH anolyte CO₂ electrolysis. *J. Phys. Chem. C* **125**, 25446–25454 (2021).
8. Rabinowitz, J. A. & Kanan, M. W. The future of low-temperature carbon dioxide electrolysis depends on solving one basic problem. *Nat. Commun.* **11**, 5231 (2020).
9. Zhang, X., Song, Y., Wang, G. & Bao, X. Co-electrolysis of CO₂ and H₂O in high-temperature solid oxide electrolysis cells: recent advance in cathodes. *J. Energy Chem.* **26**, 839–853 (2017).
10. Ramdin, M. et al. Electroreduction of CO₂/CO to C₂ products: process modeling, downstream separation, system integration, and economic analysis. *Ind. Eng. Chem. Res.* **60**, 17862–17880 (2021).
11. Wang, L. et al. Power-to-fuels via solid-oxide electrolyzer: operating window and techno-economics. *Renew. Sustain. Energy Rev.* **110**, 174–187 (2019).
12. Gurudayal, G. et al. Sequential cascade electrocatalytic conversion of carbon dioxide to C–C coupled products. *ACS Appl. Energy Mater.* **2**, 4551–4559 (2019).
13. Jouny, M., Luc, W. & Jiao, F. High-rate electroreduction of carbon monoxide to multi-carbon products. *Nat. Catal.* **1**, 748–755 (2018).
14. Romero Cuellar, N. S. et al. Two-step electrochemical reduction of CO₂ towards multi-carbon products at high current densities. *J. CO2 Util.* **36**, 263–275 (2020).
15. Zhu, P. et al. Direct and continuous generation of pure acetic acid solutions via electrocatalytic carbon monoxide reduction. *Proc. Natl Acad. Sci. USA* **118**, e2010868118 (2021).
16. Ripatti, D. S., Veltman, T. R. & Kanan, M. W. Carbon monoxide gas diffusion electrolysis that produces concentrated C₂ products with high single-pass conversion. *Joule* **3**, 240–256 (2019).
17. Nørskov, J. K. et al. Trends in the exchange current for hydrogen evolution. *J. Electrochem. Soc.* **152**, J23 (2005).
18. Zhang, Y. J., Sethuraman, V., Michalsky, R. & Peterson, A. A. Competition between CO₂ reduction and H₂ evolution on transition-metal electrocatalysts. *ACS Catal.* **4**, 3742–3748 (2014).
19. Herzog, A. et al. Operando investigation of Ag-decorated Cu₂O nanocube catalysts with enhanced CO₂ electroreduction toward liquid products. *Angew. Chem. Int. Ed.* **60**, 7426–7435 (2021).
20. García de Arquer, F. P. et al. CO₂ electrolysis to multicarbon products at activities greater than 1 A cm⁻². *Science* **367**, 661–666 (2020).
21. Lee, S. H. et al. Oxidation state and surface reconstruction of Cu under CO₂ reduction conditions from in situ X-ray characterization. *J. Am. Chem. Soc.* **143**, 588–592 (2021).
22. Verdaguer-Casadevall, A. et al. Probing the active surface sites for CO reduction on oxide-derived copper electrocatalysts. *J. Am. Chem. Soc.* **137**, 9808–9811 (2015).
23. Li, C. W., Ciston, J. & Kanan, M. W. Electroreduction of carbon monoxide to liquid fuel on oxide-derived nanocrystalline copper. *Nature* **508**, 504–507 (2014).
24. Wang, L. et al. Electrochemically converting carbon monoxide to liquid fuels by directing selectivity with electrode surface area. *Nat. Catal.* **2**, 702–708 (2019).
25. Santatiwongchai, J., Faungnawakij, K. & Hirunsit, P. Comprehensive mechanism of CO₂ electroreduction toward ethylene and ethanol: the solvent effect from explicit water–Cu(100) interface models. *ACS Catal.* **11**, 9688–9701 (2021).
26. Calle-Vallejo, F. & Koper, M. T. M. Theoretical considerations on the electroreduction of CO to C₂ species on Cu(100) electrodes. *Angew. Chem. Int. Ed.* **52**, 7282–7285 (2013).
27. Wang, L. et al. Electrochemical carbon monoxide reduction on polycrystalline copper: effects of potential, pressure, and pH on selectivity toward multicarbon and oxygenated products. *ACS Catal.* **8**, 7445–7454 (2018).

28. Garza, A. J., Bell, A. T. & Head-Gordon, M. Mechanism of CO_2 reduction at copper surfaces: pathways to C_2 products. *ACS Catal.* **8**, 1490–1499 (2018).

29. Chernyshova, I. V., Somasundaran, P. & Ponnurangam, S. On the origin of the elusive first intermediate of CO_2 electroreduction. *Proc. Natl Acad. Sci. USA* **115**, E9261–E9270 (2018).

30. Gunathunge, C. M., Ovalle, V. J., Li, Y., Janik, M. J. & Waegele, M. M. Existence of an electrochemically inert CO population on Cu electrodes in alkaline pH. *ACS Catal.* **8**, 7507–7516 (2018).

31. Oda, I., Ogasawara, H. & Ito, M. Carbon monoxide adsorption on copper and silver electrodes during carbon dioxide electroreduction studied by infrared reflection absorption spectroscopy and surface-enhanced Raman spectroscopy. *Langmuir* **12**, 1094–1097 (1996).

32. Gao, J. et al. Selective C–C coupling in carbon dioxide electroreduction via efficient spillover of intermediates as supported by operando Raman spectroscopy. *J. Am. Chem. Soc.* **141**, 18704–18714 (2019).

33. Li, J. et al. Constraining CO coverage on copper promotes high-efficiency ethylene electroproduction. *Nat. Catal.* **2**, 1124–1131 (2019).

34. Shan, W. et al. In situ surface-enhanced Raman spectroscopic evidence on the origin of selectivity in CO_2 electrocatalytic reduction. *ACS Nano* **14**, 11363–11372 (2020).

35. Fielicke, A., Gruene, P., Meijer, G. & Rayner, D. M. The adsorption of CO on transition metal clusters: a case study of cluster surface chemistry. *Surf. Sci.* **603**, 1427–1433 (2009).

36. Sandberg, R. B., Montoya, J. H., Chan, K. & Nørskov, J. K. CO–CO coupling on Cu facets: coverage, strain and field effects. *Surf. Sci.* **654**, 56–62 (2016).

37. Quilès, F. & Burneau, A. Infrared and Raman spectra of alkaline-earth and copper(II) acetates in aqueous solutions. *Vib. Spectrosc.* **16**, 105–117 (1998).

38. Bohra, D. et al. Lateral adsorbate interactions inhibit $HCOO^-$ while promoting CO selectivity for CO_2 electrocatalysis on silver. *Angew. Chem.* **131**, 1359–1363 (2019).

39. Shao, F. et al. In situ spectroelectrochemical probing of CO redox landscape on copper single-crystal surfaces. *Proc. Natl Acad. Sci. USA* **119**, e2118166119 (2022).

40. Li, F. et al. Molecular tuning of CO_2-to-ethylene conversion. *Nature* **577**, 509–513 (2019).

41. Zhu, P. & Wang, H. High-purity and high-concentration liquid fuels through CO_2 electroreduction. *Nat. Catal.* **4**, 943–951 (2021).

42. Yang, P. P. et al. Protecting copper oxidation state via intermediate confinement for selective CO_2 electroreduction to C_{2+} fuels. *J. Am. Chem. Soc.* **142**, 6400–6408 (2020).

43. Luc, W. et al. Two-dimensional copper nanosheets for electrochemical reduction of carbon monoxide to acetate. *Nat. Catal.* **2**, 423–430 (2019).

44. Martić, N. et al. $Ag_2Cu_2O_3$–a catalyst template material for selective electroreduction of CO to C_{2+}. products. *Energy Environ. Sci.* **13**, 2993–3006 (2020).

Acknowledgements

Author contributions

E.H.S. supervised the project. R.D., I.G. and B.-H.L. conceived the idea. R.D., B.-H.L. and I.G. designed and performed the experiments. R.D., with the help of P.O., carried out the DFT calculations. J.A. performed the XAS experiments. J.A., I.G. and R.D. analysed the XAS data. A.S.R. performed the XPS experiments. A.S.R. and I.G. analysed the XPS data. M.P., B.-H.L. and R.D. performed the TEM and SEM measurements. R.K.M., E.S., J.W., S.P., G.L. and J.Z. contributed to the data interpretation, material synthesis and characterization. R.K.M., C.O. and D.S. assisted with the electrochemical system design. R.D., I.G., B.-H.L., P.O. and E.H.S. wrote the manuscript. All the authors commented on the manuscript.

Competing interests

The authors declare no competing interests.

Additional information

Supplementary information The online version contains supplementary material available at https://doi.org/10.1038/s44160-023-00259-w.

Correspondence and requests for materials should be addressed to Edward H. Sargent.

Peer review information *Nature Synthesis* thanks Dehui Deng and the other, anonymous, reviewer(s) for their contribution to the peer review of this work. Primary Handling Editor: Alexandra Groves, in collaboration with the *Nature Synthesis* team.

Reprints and permissions information is available at www.nature.com/reprints.